POLISH MARITIME RESEARCH 2 (118) 2023 Vol. 30; pp. 11-27
10.2478/pomr-2023-0018

NUMERICAL ANALYSIS OF RESISTANCE CHARACTERISTICS OF A NOVEL HIGH-SPEED QUADRAMARAN

Xin Liu
Jimei University, School of Marine Engineering, Xiamen, China
Jinglei Yang
Jimei University, School of Marine Engineering, Xiamen, China
Defeng Wu
Jimei University, School of Marine Engineering, Xiamen, China
Liang Hou
Shanghai Xiyi Marine Technology Co., Ltd, Shanghai, China
Xiaowen Li
Jimei University, School of Marine Engineering, Xiamen, China
Qian Wan
Dalian Shipbuilding Industry Co., Ltd, Dalian, China

* Corresponding author: *yangjinglei1220@126.com (Jinglei Yang)*

ABSTRACT

This paper utilised computational fluid dynamics (CFD) technology to calculate the resistance of a novel high-speed quadramaran in calm water using the Navier–Stokes (N–S) equation, analysed the total resistance, frictional resistance, and residual resistance characteristics of this novel high-speed quadramaran at different length Froude numbers, and compared them with the results of a conventional high-speed catamaran with the same displacement. The results showed that the total resistance of the quadramaran had a significant hump at the Froude number of 0.6, due to the complexity of the wave interference among the four demihulls, and the hump value was about 1.6 times that of the catamaran. Above the hump speed, the total resistance of the quadramaran decreased with the increase of the Froude number, until reaching the Froude number of 1.06, when the curve became flat, and it showed a maximum resistance reduction of 40% at the Froude number of 1.66 compared with the catamaran, where the total resistance curve was steep. The frictional resistance of the quadramaran increased gradually with the growth of the Froude number, which was basically consistent with the change trend of the catamaran. The residual resistance of the quadramaran first rose and then reduced with the rising Froude number, the curve showed a large hump due to the adverse wave interference, and the hump value was about 1.7 times that of the catamaran. Above the Froude number of 1.06, as the wave interference changed from adverse to favourable, the quadramaran had lower residual resistance than the catamaran. The bow and stern demihulls of the quadramaran were also analysed for their resistance characteristics. The total resistance of the bow demihulls increased gradually with the increase of the Froude number, the curve had a small hump at the Froude number of 0.7, and above the hump speed, the curve was steep. The total resistance of the stern demihulls first increased and then decreased with the growth of the Froude number, the hump value at the Froude number of 0.85 was significant and was about 2 times that of the bow demihulls, and the curve became flat above the Froude number of 1.51.

Keywords: high-speed quadramaran; high-speed catamaran; resistance characteristic; wave-making interference; resistance hump

INTRODUCTION

In recent years, multi-hulls have been widely studied by a large number of researchers because of their wide deck area, excellent speed, and seakeeping performance. The catamaran is one of the most widely studied and applied hull forms, with relatively variable designs, including the small waterline catamaran (SWATH), wave-piercing catamaran, partial air cushion support catamaran (PACSCAT) [1–2], asymmetric catamaran [3–5], supercritical catamaran [6], etc. Trimarans and pentamarans mostly use the form of a large main hull in the middle and small demihulls distributed on both sides of the main hull, while the hull forms are mostly slender or small waterline hulls. However, there is not much research on the quadramaran, and most researchers who study quadramarans generally take slender or small waterline hulls as the hull forms. Peng [7] utilised the boundary element method in terms of the Green function to compute the resistance and motion responses of a slender catamaran, trimaran, quadramaran, and pentamaran by altering the configurations of the demihulls. Fang et al. [8] took the small waterline quadramaran (SLICE) as the research object to investigate its resistance characteristics, compared with a SWATH of the same scale, and concluded that the SLICE had certain resistance advantages only under the condition of shallow draft. Michell's linear wave resistance theory method was adopted by Cai et al. [9] to study the wave-making resistance characteristics of a SWATH, trimaran, SLICE, and pentamaran at different Froude numbers, and obtain the proportion of wave-making resistance. A series of numerical simulations based on FLUENT software was performed by Zhang et al. [10], and the total resistance characteristics and flow field distributions of a small waterline catamaran, trimaran, and quadramaran were analysed. Based on Neumann–Michell theory, Liu et al. [11] used the self-developed NMShip-SJTU solver to numerically calculate the wave-making resistance of a staggered quadramaran with slender demihulls at different Froude numbers and different longitudinal and transverse positions, analysing the wave interference characteristics. Yanuar et al. [12-13] conducted a set of experiments in calm water to investigate the effect of the quadramaran configurations on the total resistance coefficient and interference factor.

As a prominent research method, computational fluid dynamics (CFD) technology is widely applied by many researchers in the process of ship design, and can accurately and effectively forecast the hydrodynamic performance of ships. Farkas et al. [14] performed a number of numerical simulations of an S60 catamaran at different separations to obtain the characteristics of the total resistance and the wave interference factor, and the numerical results showed good agreement with the experimental results. Hu et al. [15] developed an asymmetric catamaran and investigated its resistance, rise-up, and dynamic trim angle by altering the lateral separation and longitudinal stagger based on the CFD method, and the deviations of the numerical results from the experimental results were less than 6%. Ebrahimi et al. [16] proposed a planing catamaran with transverse steps, analysed the aero-hydrodynamic effect in calm water at different displacements, and numerically calculated the resistance, the results of which agreed well with the experimental data. Li et al. [17] investigated the seakeeping characteristics of a slender trimaran equipped with and without a T-foil near the bow by experimental and numerical methods. The numerical simulations were validated by comparisons with the experimental tests. A range of numerical simulations were carried out by Heidari et al. [18], and the effects of the trim, heel, and yaw angles of the side hulls on the resistance and flow field characteristics of a trimaran were investigated; by contrast with the experimental values, the maximum numerical error was only 5%. Yildiz et al. [19] analysed the total resistance and wave profiles of a trimaran with nine different outrigger configurations by using the CFD method, and obtained good agreements when compared with the experimental results. To reduce the resistance in calm water and wavy conditions, Nazemian et al. [20] took the numerical results as the objective function, which were computed by CFD simulation and matched well with the experimental data, and utilised an arbitrary shape deformation method to optimise the hull shape of a wave-piercing trimaran. All the studies mentioned above applied the STAR CCM+ solver to perform numerical calculations, and good consistencies were shown between the numerical and experimental results, which verified the validity of the CFD method. So, this indicates that the CFD method could meet the requirements of practical engineering applications and reliably and accurately predict the hydrodynamic performance of multi-hulls.

In this paper, a novel high-speed quadramaran with a service speed above 30 kn is developed. A high-speed V-shaped hull form is applied to the demihull, which is different from the slender or small waterline quadramaran studied by previous researchers. It is undeniable that the slender hull or small waterline hull is conducive to reducing the wave-making resistance of multi-hulls, but the draft of the hull at the same displacement is deep, which is not conducive to navigating in a shallow fairway and is detrimental to the development of the hull form towards heavy loads and large sizes. Compared with a slender hull, the shape of the demihull makes the hull space more spacious, facilitates the arrangement of equipment, and makes the draft shallower. As the most widely used, the V-shaped hull form has excellent high-speed performance, but its seakeeping performance is unsatisfactory in a rough sea state. The advantage of multi-hulls is that they have great seakeeping and stability performance in rough sea states, but the wave-making resistance will be larger than that of monohulls due to the wave interference among the demihulls at high speed. The ship type proposed is based on the quick reach needs of windfarm maintenance and ocean transportation, which require a service speed above 30 kn. The hull form integrates the advantages of the V-shaped hull and multi-hull, which means that the quadramaran has not only a remarkable high-speed performance, but also excellent seakeeping in rough sea states. This paper studies the resistance characteristics

of the quadramaran in calm water, including the resistance, rise-up, dynamic trim angle, and wave-making interference. Analyses are carried out with several numerical simulations based on the mature STAR CCM+ solver. The computed results could provide data support for the further study of ship model experiments.

NUMERICAL SIMULATION METHOD

GOVERNING EQUATIONS AND THEORIES

Considering the influence of turbulent pulsation, the governing equations of fluids are commonly based on the time-averaged method [21–22]. The continuous equation and the Reynolds-Averaged Navier–Stokes equation are expressed as follows:

$$\frac{\partial \rho}{\partial t} + \frac{\partial}{x_i}(\rho u_i) = 0 \quad (1)$$

$$\frac{\partial(\rho u_i)}{\partial t} + \frac{\partial}{\partial x_j}(\rho u_i u_j) = -\frac{\partial P}{\partial x_i} + \frac{\partial}{\partial x_j}\left(\mu \frac{\partial u_i}{\partial x_j} - \overline{\rho u_i' u_j'}\right) + S_i \quad (2)$$

where u_i and u_j are the time-averaged value of the velocity component, and the value range of subscript i and j is (1,2,3); P is the time-averaged value of the pressure; ρ is the fluid density; μ is a hydrodynamic viscosity coefficient; $-\overline{\rho u_i' u_j'}$ is the Reynolds stress; and S_i is the generalised source term of the momentum equation.

The standard $k-\varepsilon$ model is used as the turbulence model in this paper. The equation of the turbulent kinetic energy k and turbulent dissipation rate ε are expressed as follows:

$$\frac{\partial(\rho k)}{\partial t} + \frac{\partial(\rho k u_i)}{\partial x_i} = \frac{\partial}{\partial x_j}\left[\left(\mu + \frac{\mu_t}{\sigma_k}\right)\frac{\partial k}{\partial x_j}\right] + G_k - \rho\varepsilon \quad (3)$$

$$\frac{\partial(\rho \varepsilon)}{\partial t} + \frac{\partial(\rho \varepsilon u_i)}{\partial x_i} = \frac{\partial}{\partial x_j}\left[\left(\mu + \frac{\mu_t}{\sigma_\varepsilon}\right)\frac{\partial \varepsilon}{\partial x_j}\right] + C_{1\varepsilon}\frac{\varepsilon}{k}G_k - C_{2\varepsilon}\rho\frac{\varepsilon^2}{k} \quad (4)$$

where G_k is the generation term of turbulent kinetic energy k caused by the average velocity gradient; $\mu_t = \rho C_\mu \frac{k^2}{\varepsilon}$; C_μ=0.09; σ_k=1.0; and σ_ε=1.3.

The volume of fluids (VOF) method [23–24] was utilised to capture the free liquid surface. The phase distribution and position at the interface are described by the field of phase volume fraction a_j, where the phase j is defined as follows:

$$a_j = \frac{V_i}{V} \quad (5)$$

where V_i is the volume of the phase j in the mesh cell and V is the volume of the mesh cell.

The sum of the volume fractions of all the phases in a mesh cell must be 1; that is, $\sum_{i=1}^{N} a_i = 1$, where N is the total number of phases. According to the value of the volume fraction, it can distinguish whether there are different phases or fluids in the mesh cell; that is, when a_i=0, the mesh cell has no phase i at all. When a_i=1, this mesh cell is completely filled by the phase i; $0 < a_i < 1$, where the value between the two limits indicates the existence of an interface between the phases.

COMPUTATIONAL MODEL

The ship type studied in this paper was inspired by a catamaran with a step [16]. Using a step on the hull could separate the water, create a dry section from step to transom, and reduce the resistance at high speed [25–26]. The stepped hull is viewed as two regular hulls following each other closely, so that the catamaran turns into a quadramaran. A high-speed V-shaped catamaran (Fig. 1b) is selected to separate at midship, the first demihulls are used as the bow demihulls of the quadramaran, and the second demihulls are replaced by other V-shaped hulls used as the stern demihulls of the quadramaran, where the centre lines of the bow and stern demihulls are aligned. Before the ship type in this paper was proposed, a hull form optimisation study was carried out, and it was found that a large deadrise angle at the bow demihull was beneficial to improve the wave interference and reduce the total resistance. So that the bow and stern demihulls are of different V-shaped hull forms, the bow hull has leaner lines, larger deadrise angles, and smaller waterline entrance angles than those of the stern hull.

A full-scale model has been chosen as the study objective, and the main parameters of the catamaran and quadramaran in full scale are listed in Table 1. They have the same displacement and same waterline length, and the geometry models are established as shown in Fig. 1.

Tab. 1 The main parameters of the quadramaran and catamaran

High-speed quadramaran		High-speed catamaran	
Parameters	Value	Parameters	Value
Length overall of bow demihull L_{bOA} (m)	11.76	Length overall of demihull L_{OA} (m)	22.5
Length overall of stern demihull L_{sOA} (m)	12.32		
Waterline length of bow demihull L_b (m)	11.00	Waterline length of demihull L (m)	21.72
Waterline length of stern demihull L_s (m)	10.72		
Moulded breadth of bow demihull B_b (m)	3.92	Moulded breadth of demihull B (m)	3.38
Moulded breadth of stern demihull B_s (m)	4.1		
Deadrise angle in the midship of bow demihull β_b (°)	40.9	Deadrise angle in the midship of demihull β (°)	27.3
Deadrise angle in the midship of stern demihull β_s (°)	18.9		

High-speed quadramaran		High-speed catamaran	
Parameters	Value	Parameters	Value
Transverse spacing of the centreline of demihulls K_c (m)	5.55	Transverse spacing of the centreline of demihulls K_c (m)	5.2
Longitudinal spacing of demihulls K_l (m)	0.05	Longitudinal spacing of demihulls K_l (m)	/
Length overall of quadramaran L_{OA} (m)	24.13	Length overall of catamaran L_{OA} (m)	22.5
Breadth overall of quadramaran B_{OA} (m)	9.65	Breadth overall of catamaran B_{OA} (m)	8.44
Moulded depth D (m)	2.4	Moulded depth D (m)	3.5
Draft T (m)	1.13	Draft T (m)	1.2
Displacement of bow demihulls Δ_b (t)	27	Displacement of bow demihulls Δ_b (t)	/
Displacement of stern demihulls Δ_s (t)	43	Displacement of stern demihulls Δ_s (t)	/
Total displacement of quadramaran Δ (t)	70	Total displacement of catamaran Δ (t)	70

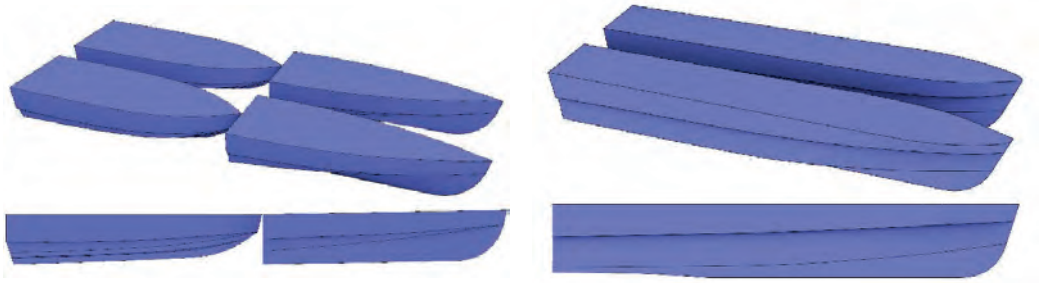

(a) quadramaran *(b) catamaran*

Fig. 1. The geometry models

NUMERICAL SCHEME

Boundary conditions

The computational domain is extended 1.5 L to the front of the bow, 3 L to the rear of the stern, L to the side, L above the free surface, and 1.5 L below the free surface. The boundary conditions of the inlet, top, and bottom of the computational domain are set as the velocity inlet, the outlet is set as the pressure outlet, both sides are set as the symmetry plane, and the hull surface is set as a no-slip wall surface.

Calculation setup

The implicit unsteady state is selected as the time model, the material is selected as Euler multiphase flow, the motion of the hull is set as six degrees of freedom rigid body motion, the VOF wave is set as calm water, the time step is set to 0.001 s, and the iteration step is 10 steps.

The studied speed ranges between 3.6 m/s and 24.18 m/s, because the total waterline length of the quadramaran, that is, the sum of the bow and stern demihulls' waterline length, is the same as that of the catamaran, so that they have the same length Froude number, represented by the symbol F_r. Besides, the symbols F_{rb} and F_{rs} represent the length Froude number of the bow and stern demihull, respectively. Table 2 shows the corresponding speeds of the computational model.

Tab. 2 Corresponding speeds of computational model

Speed V (m/s)	Speed V (kn)	Length Froude number of entire hull F_r	Volume Froude number of entire hull $F_{r\nabla}$	Length Froude number of bow demihull F_{rb}	Length Froude number of stern demihull F_{rs}
3.60	7	0.25	0.41	0.35	0.35
5.14	10	0.35	0.57	0.50	0.50
6.69	13	0.46	0.81	0.64	0.65
7.72	15	0.53	1.06	0.74	0.75
8.74	17	0.60	1.22	0.84	0.85
10.29	20	0.71	1.38	0.99	1.00
11.83	23	0.81	1.63	1.14	1.15
12.86	25	0.88	1.87	1.24	1.25
13.89	27	0.95	2.03	1.34	1.36
15.43	30	1.06	2.19	1.49	1.51
16.98	33	1.17	2.44	1.64	1.66
18.00	35	1.23	2.69	1.73	1.76
19.03	37	1.30	2.84	1.83	1.86
20.58	40	1.41	3.01	1.98	2.01
22.12	43	1.52	3.25	2.13	2.16
23.15	45	1.59	3.49	2.23	2.26
24.18	47	1.66	3.66	2.33	2.36

Grid convergence study

To boost confidence in the CFD computation results, a grid convergence study is needed before systematic computations according to ITTC recommended procedures [27-28]. Three sets of grids corresponding to fine, medium, and coarse grids are established, respectively. The grid refinement ratio is $r_G = \sqrt{2}$. Taking the quadramaran speed 20.58 m/s as an example, the grids from the finest to the coarsest grids are illustrated in Fig. 2, and the grid cell numbers are given in Table 3. The calculated results using different grid strategies are shown in Table 4.

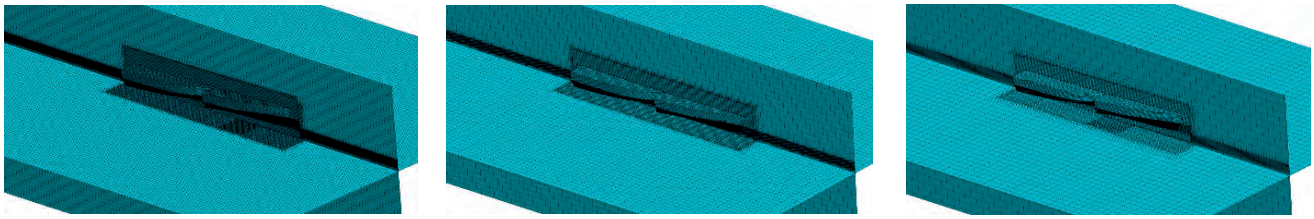

(a) fine grid *(b) medium grid* *(c) coarse grid*

Fig. 2. Grids from finest to coarsest

Tab. 3 Number of cells for three grids

Grid scheme	(a) fine grid S_1	(b) medium grid S_2	(c) coarse grid S_3
Number of grids	38775148	16133326	6091183

Tab. 4 Calculated results using different grid strategies

Grid scheme	(a) fine grid S_1	(b) medium grid S_2	(c) coarse grid S_3
Bow total resistance (kN)	43.40	44.18	45.17
Stern total resistance (kN)	39.64	41.26	43.61
Total resistance (kN)	83.08	85.46	88.77
Dynamic trim angle (°)	1.397	1.427	1.469
Rise-up (m)	0.418	0.419	0.421

Tab. 5 Grid uncertainty analysis

Grid scheme	Bow total resistance	Stern total resistance	Total resistance	Dynamic trim angle	Rise-up
Convergence ratio R_G	0.787	0.686	0.718	0.697	0.451
Convergence condition	Monotonic	Monotonic	Monotonic	Monotonic	Monotonic
Accuracy P_G	0.693	1.086	0.957	1.042	2.298
Grid error $\delta^*_{RE_G}$	2.867	3.529	6.042	0.068	0.0007
Correction factor C_G	0.271	0.457	0.393	0.435	1.218
$\|1 - C_G\|$	0.729	0.543	0.607	0.565	0.218
Uncertainty U_G	7.045	7.363	13.376	0.145	0.0099
Uncertainty $U_G(\% S_G)$	16.23%	18.57%	16.10%	10.34%	0.24%
Correction error δ^*_G	0.778	1.613	2.375	0.0295	0.0008
Correction error $\delta^*_G(\% S_G)$	1.83%	4.24%	2.94%	2.16%	0.20%
Correction uncertainty U_{C_G}	2.089	1.917	3.667	0.038	0.0001
Correction uncertainty $U_{G_C}(\% S_G)$	4.90%	5.04%	4.54%	2.80%	0.04%

The differences in the results between the different grid schemes are defined as follows:

$$\begin{cases}\varepsilon_{21} = S_2 - S_1 \\ \varepsilon_{32} = S_3 - S_2\end{cases} \quad (1)$$

The convergence ratio R_G is defined as

$$R_G = \frac{\varepsilon_{21}}{\varepsilon_{32}} \quad (2)$$

According to [27], three convergence conditions are possible:
(1) Monotonic convergence: $0 < R_G < 1$;
(2) Oscillatory convergence: $R_G < 0$;
(3) Divergence: $R_G > 1$.

The results of the convergence ratio R_G shown in Table 5 are less than 1, so the grid convergence is monotonic.

For monotonous convergence, the Generalized Richardson extrapolation is used to estimate the grid error $\delta^*_{RE_G}$.

$$\delta^*_{RE_G} = \frac{\varepsilon_{21}}{r_G^{P_G} - 1} \quad (3)$$

The order of accuracy P_G is estimated as

$$P_G = \frac{In\left(\varepsilon_{32}/\varepsilon_{21}\right)}{In(r_G)} \quad (4)$$

The correction factor C_G is defined as

$$C_G = \frac{r_G^{P_G} - 1}{r_G^{P_{Gest}} - 1} \quad (5)$$

where $P_{Gest} = 2$ was used according to [28].

For C_G considered as sufficiently less than or greater than 1 and lacking confidence, the error δ_G is not estimated, and the uncertainty U_G is estimated as follows:

$$U_G = \begin{cases}[9.6(1 - C_G)^2 + 1.1]\left|\delta^*_{RE_G}\right| & |1 - C_G| < 0.125 \\ [2|1 - C_G| + 1]\left|\delta^*_{RE_G}\right| & |1 - C_G| \geq 0.125\end{cases} \quad (6)$$

For C_G considered close to 1 and having confidence, the correction error δ^*_G and the correction uncertainty U_{G_C} are estimated as follows:

$$\delta^*_G = C_G \delta^*_{RE_G} \quad (7)$$

$$U_{G_C} = \begin{cases}[2.4(1 - C_G)^2 + 0.1]\left|\delta^*_{RE_G}\right| & |1 - C_G| < 0.25 \\ [|1 - C_G|]\left|\delta^*_{RE_G}\right| & |1 - C_G| \geq 0.25\end{cases} \quad (8)$$

The correction simulation result S_C is defined as

$$S_C = S_G - \delta^*_G \quad (9)$$

where S_G is the result of numerical simulation under the finest grid S_1.

Table 5 shows the results of the grid uncertainty analysis. δ^*_G and U_{G_C} are relatively small, so the level of verification is relatively small, < 6%. This indicates that the errors in the results caused by grid discretisation are very small. Thus, as a trade-off between accuracy and efficiency, the grid density S_2 is selected for calculation.

Mesh generation

The overset mesh method is applied to the computational mesh. Mesh encryption is performed on the free liquid surface and the area around the hull, respectively, and boundary layer meshes are set around the hull, where 6 boundary layers are created with a growth rate of 1.1. The specific computational meshes are shown in Fig. 3. The y+ distribution obtained for the speed of 20.58 m/s from the full-scale simulation is shown in Fig. 4, where the value for y+ around the hull is about 100–1500.

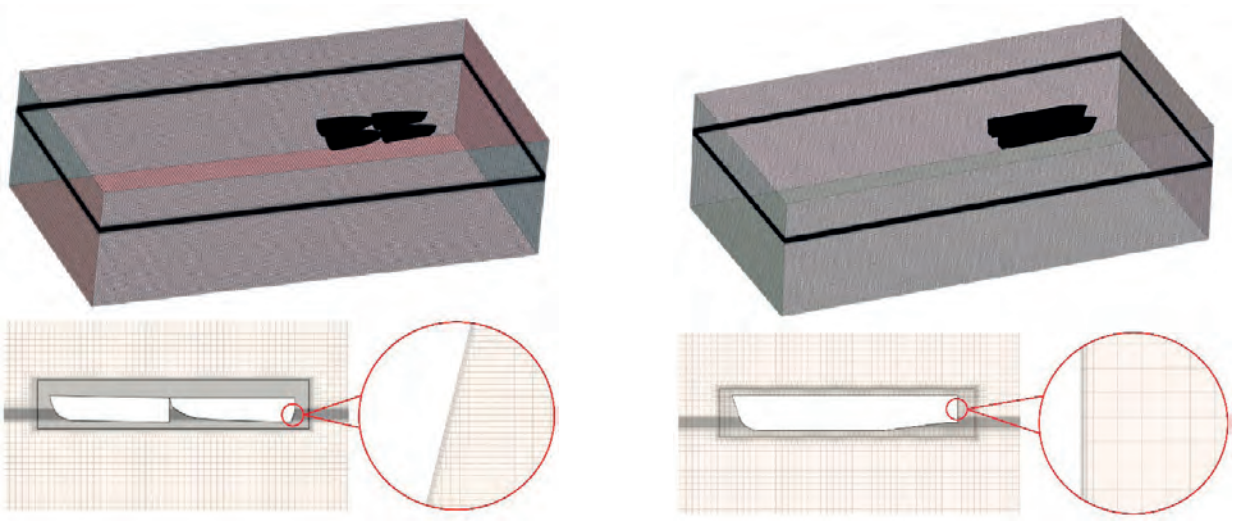

(a) quadramaran *(b) catamaran*

Fig. 3. Computational mesh

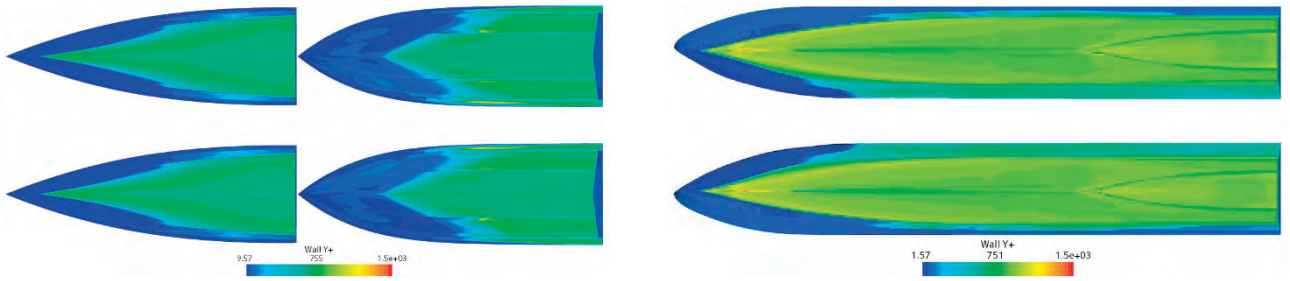

(a) quadramaran *(b) catamaran*

Fig. 4. The distribution of y+ for the speed of 20.58 m/s

Validation of the numerical method

Considering the absence of publicly available ship model test results, a V-shaped high-speed boat from the M_1 ship type proposed by Parviz Ghadimi [26] is selected to carry out a comparative study to assess the accuracy of the numerical methods. Table 6 lists the principal dimensions of hull M_1 while Fig. 5 illustrates the geometry of the model.

The results are compared with experimental and CFD data for the total resistance, dynamic trim angle and rise-up, as given in Figs. 6–8. It is seen that the numerical results of the total resistance and dynamic trim angle agree well with the experimental results. The maximum deviation of the total resistance is 10.9% at 7 m/s, and the maximum deviation of the dynamic trim angle is 18.76% at 7 m/s. Although the overall deviation of the rise-up is large, the general trend is consistent with the experimental value. It can be seen that the CFD numerical calculation method used in this paper is suitable and has reliable calculation accuracy.

Tab. 6 The principal dimensions of hull

Parameters	Value
Length overall L_{OA} (m)	2.64
Maximum beam B (m)	0.551
Displacement Δ (kg)	86
Longitudinal distance of gravity centre L_{CG} (m)	0.791
Vertical distance of gravity centre V_{CG} (m)	0.185
Speed V (m/s)	1–7

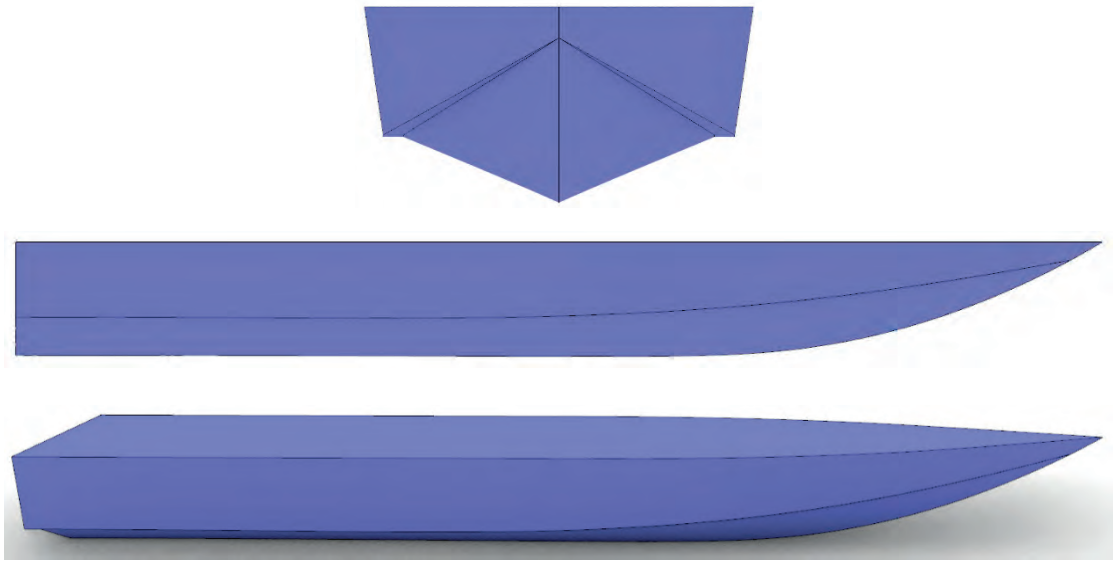

Fig. 5. The geometry of the model

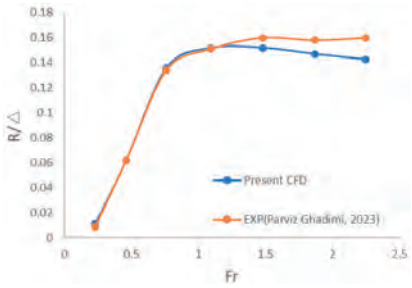

Fig. 6. Comparison of total resistance

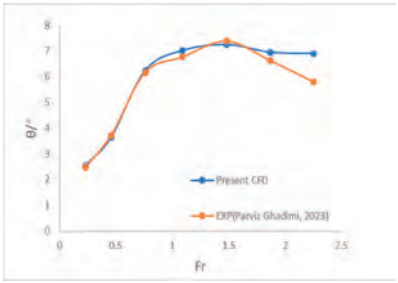

Fig. 7. Comparison of dynamic trim angle

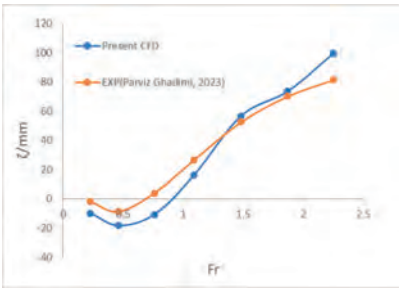

Fig. 8. Comparison of rise-up

CALCULATION RESULTS AND ANALYSIS

For high-speed ships, resistance can be divided into two parts: frictional resistance and residual resistance [29]. The calculation formula of the total resistance is expressed as follows.

$$R_t = C_t \frac{1}{2}\rho S V^2 \tag{10}$$

where C_t is the total resistance coefficient, $C_t = C_f + C_r + \Delta C_F$; C_f is the frictional resistance coefficient; C_r is the residual resistance coefficient; ΔC_F is the correction coefficient, which is 0.0004; ρ is the density of seawater, kg/m^3; S is the wet surface area of the hull, m^2; V is the hull speed, m/s.

The frictional resistance coefficient C_F is obtained based on the equivalent plank assumption, which was determined by the International Towing Tank Conference (ITTC) [30], that is:

$$C_f = \frac{0.075}{(\lg Re - 2)^2} \tag{11}$$

where Re is the Reynolds number.

For high-speed ships, although the viscous pressure resistance accounts for a small proportion of the residual resistance, most of the residual resistance is composed of the wave-making resistance, so the characteristics of the wave-making resistance can be reflected by the residual resistance [31].

According to [32], when the length Froude number $F_r < 0.4$, the buoyancy force dominates relative to the hydrodynamic force effect, and vessels in this Froude number range are called displacement vessels; vessels with a length Froude number in the range of $0.4 - 0.5 < F_r < 1.0 - 1.2$ are called semi-planing vessels, which means that high-speed submerged hull-supported vessels denote vessels in which the buoyancy force is not dominant; vessels with a length Froude number in the range of $F_r > 1.0 - 1.2$ are called planing vessels, which means that the hydrodynamic force mainly carries the weight. However, there is no clear line of demarcation between planing and nonplaning conditions just by referring to the length Froude number, as individual circumstances alter cases.

In this paper, the calculation results were analysed by using non-dimensional parameters. The speed is represented by the length Froude number F_r, which is defined as $F_r = \frac{V}{\sqrt{gL}}$, and the resistance is represented by the resistance to weight ratio, which is defined as R/Δ, where V is the hull speed, m/s L is the waterline length, m; g is the acceleration of gravity, with a value of 9.8 m/s^2; R is the resistance value, N; and Δ is the hull weight, kg.

ANALYSIS OF RESISTANCE CHARACTERISTICS OF INTEGRATED HULL

Figs. 9–13 show the comparison curves of the characteristics of the rise-up ζ, dynamic trim angle θ, frictional resistance R_f/Δ , residual resistance R_r/Δ and total resistance R_t/Δ of the quadramaran and catamaran as a function of the length Froude number F_r, respectively.

From the curves of the quadramaran, it can be seen that at low speed ($F_r < 0.53$), the motion turns from the displacement regime into the semi-planing regime, the dynamic trim angle increases with the increase of , the bow rises and the stern descends, so the rise-up is negative. The frictional resistance, residual resistance, and total resistance increase constantly. Because the hydrodynamic force is not enough to support the hull in this regime, the dynamic trim angle keeps increasing and the hull keeps descending until reaching the Froude number of 0.53, when the curve of the rise-up shows its hump, and the hull begins to rise. The dynamic trim angle, the residual resistance, and the total resistance have a significant hump at the Froude number of 0.6. Above the hump speed, due to the hydrodynamic force effect, the dynamic trim angle, the residual resistance, and the total resistance begin

to decrease until reaching the Froude number of 1.06, when the motion enters the planing regime, the dynamic trim angle becomes relatively steady, and the rise-up continues to increase gradually due to the hydrodynamic force effect. So the residual resistance keeps decreasing, while, because of the rapid growth of frictional resistance, the total resistance curve becomes remarkably flat and shows no upward trend.

Fig. 9 shows the comparison between the rise-up curves of the quadramaran and catamaran, where it can be seen that the two hulls have roughly the same change trend. Both hulls first descend and then rise, and both have a large hump at the Froude number of 0.53. However, because the quadramaran makes the flow separate from the middle and generates multiple planing surfaces leading to the hydrodynamic force being multiplied and greater, the rise-up value of the quadramaran is significantly higher than that of the catamaran.

Fig. 10 presents the comparison between the dynamic trim angle curves of the quadramaran and catamaran. It can be seen that both hulls also have roughly the same change trend. The dynamic trim angle of the two hulls first increases and then decreases; the quadramaran shows the hump at the Froude number of 0.6, while the catamaran shows the hump at the Froude number of 0.53. Because the bow and stern demihulls of the quadramaran generate multiple planing surfaces, causing the hydrodynamic force to be decentralised rather than concentrated like the catamaran, the angle amplitude of the catamaran is greater than that of the quadramaran, which is the opposite of the curve of the rise-up due to the special ship type.

Fig. 11 illustrates that the frictional resistance curves of both hulls have similar change trends on account of the similar main scales of the hulls.

Fig. 12 shows the comparison between the residual resistance curves of the quadramaran and catamaran. At low speed ($F_r < 0.53$), the residual resistance of both hulls increases constantly with the growth of F_r. The catamaran shows the hump at the Froude number of 0.53, while the quadramaran shows the hump at the Froude number of 0.6. The complexity of the wave interference among the four demihulls leads to the quadramaran having a significant hump, the value of which is about 1.7 times that of the catamaran. Above the hump speed, the residual resistance of both hulls reduces until reaching the Froude number of 1.06. The adverse wave interference makes the residual resistance of the catamaran increase again, while the residual resistance of the quadramaran continues to decrease due to the increase of the rise-up and the occurrence of favourable wave interference.

Fig. 13 shows the comparison between the total resistance curves of the quadramaran and catamaran. At low speed ($F_r < 0.53$), the two hulls turn from the displacement regime into the semi-planing regime, and the total resistance of both hulls increases constantly with the growth of F_r. The catamaran shows the hump at the Froude number of 0.53, while the quadramaran shows the hump at the Froude number of 0.6. The complexity of the wave interference among the four demihulls leads to the quadramaran having a significant hump, the value of which is about 1.6 times that of the catamaran. Above the hump speed, the total resistance of the catamaran still increases gently, while the quadramaran begins to decrease, until reaching the Froude number of 1.06, when the two hulls enter the planing regime, and the total resistance of the catamaran increases steeply, while for the quadramaran it becomes flat. Above the Froude number of 1.06, the quadramaran starts to have less total resistance than the catamaran, with a maximum resistance reduction of 40% at the Froude number of 1.66. This indicates that the quadramaran has a remarkable resistance advantage above the Froude number of 1.06 (at a service speed above 30 kn).

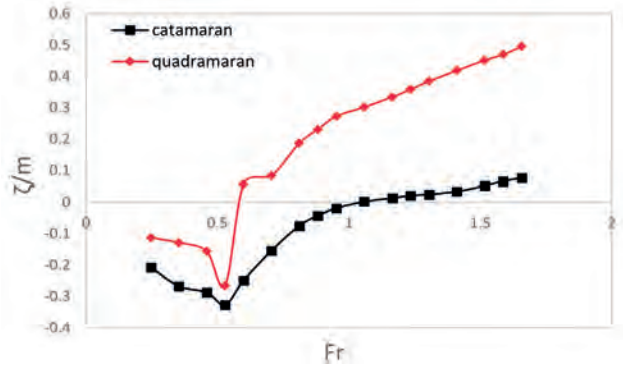

Fig. 9. Comparison of curves of rise-up

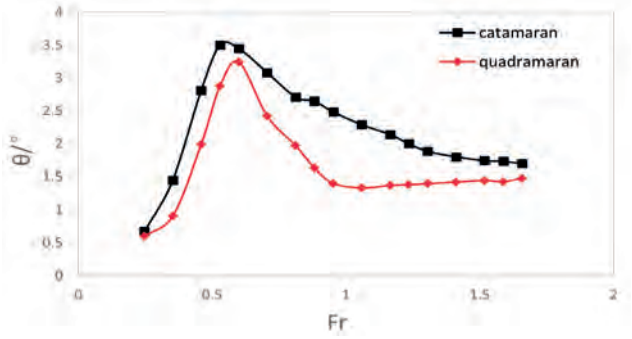

Fig. 10. Comparison of curves of dynamic trim angle

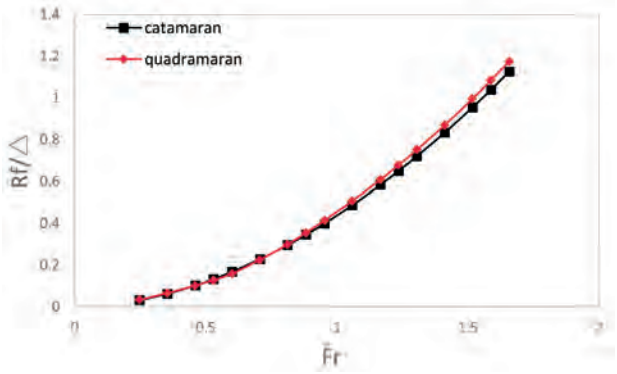

Fig. 11. Comparison of curves of frictional resistance

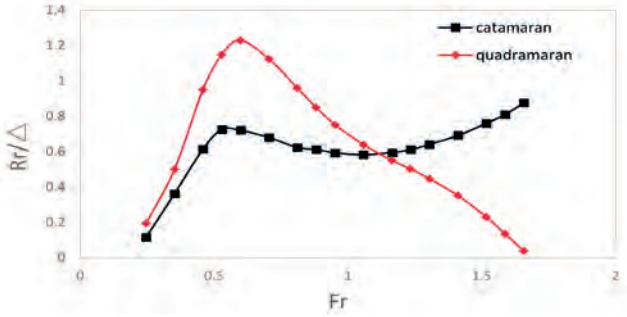

Fig. 12. Comparison of curves of residual resistance

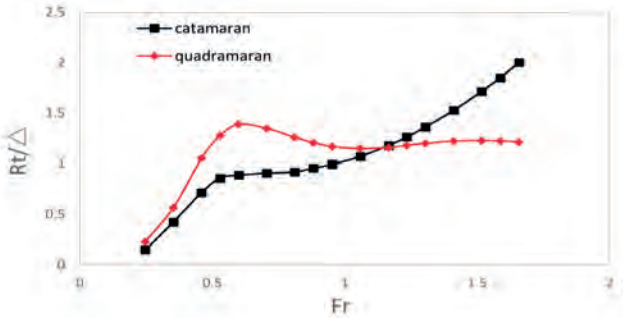

Fig. 13. Comparison of curves of total resistance

ANALYSIS OF RESISTANCE CHARACTERISTICS OF DEMIHULLS

The resistance of the demihulls is monitored independently by decomposing from the quadramaran hull. Figs. 14–19 show the resistance calculation results of the bow and stern demihulls of the quadramaran, in which the lower corner labels b and s represent the bow and stern, respectively.

Figs. 14 and15 present the frictional resistance curves of the bow and stern demihulls. It can be seen that the trends of frictional resistance of the bow and stern demihulls change similarly, as both increase constantly with the increase of the Froude number, which reflects that the frictional resistance is directly proportional to the square of speed. The leaner hull form, leading to a smaller wetted surface, makes the bow demihulls have lower values of frictional resistance.

Figs. 16 and 17 show the residual resistance curves of the bow and stern demihulls. At low speed (V < 7.72 m/s), the residual resistance of both demihulls rises gradually with the growth of the Froude number. The bow demihulls show the hump at the Froude number of 0.74, while the stern demihulls show the hump at the Froude number of 0.85. The reason is that the stern demihulls are located in the flow field of the bow demihulls, so the complexity of the wave interference makes the stern have a significant hump, the value of which is about 2 times that of the bow demihulls. Above the hump speed, as the hull rises, the residual resistance of both demihulls decreases with the increase of the Froude number.

Figs. 18 and 19 illustrate the total resistance curves of the bow and stern demihulls. At low speed (V < 7.72 m/s), the total resistance of both demihulls rises gradually with the growth of the Froude number. The bow demihulls show the hump at the Froude number of 0.74, while the stern demihulls show the hump at the Froude number of 0.85. The complexity of the wave interference makes the stern have a significant hump, the value of which is about 1.8 times that of the bow demihulls. Above the hump speed, the total resistance of the bow demihulls keeps increasing, while the total resistance of the stern demihulls begins to decrease until reaching the Froude number of 1.51, at which the hull enters planing mode and the curve becomes flat.

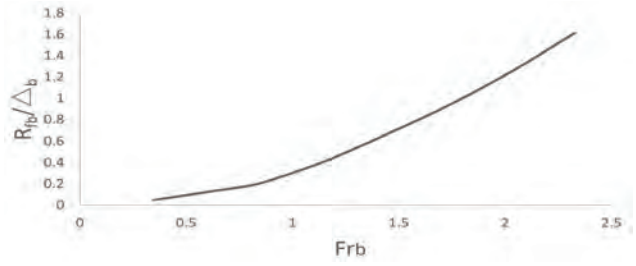

Fig. 14. Frictional resistance curve of bow demihulls

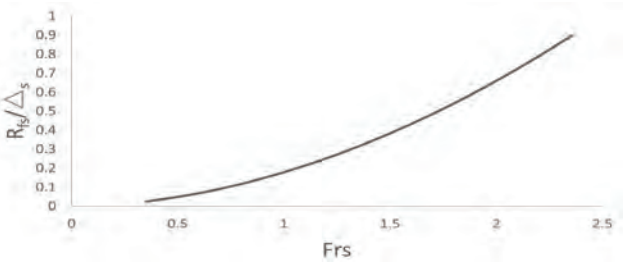

Fig. 15. Frictional resistance curve of stern demihulls

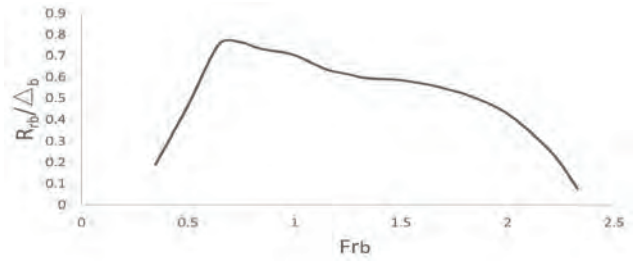

Fig. 16. Residual resistance curve of bow demihulls

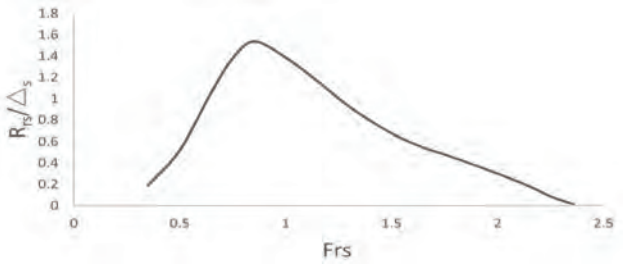

Fig. 17. Residual resistance curve of stern demihulls

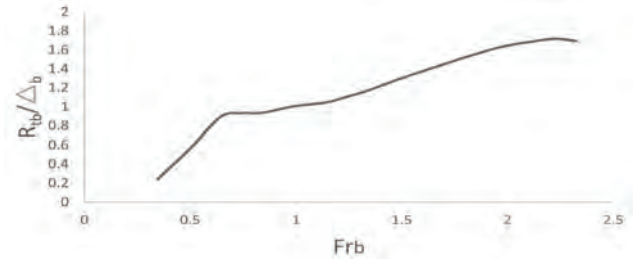

Fig. 18. Total resistance curve of bow demihulls

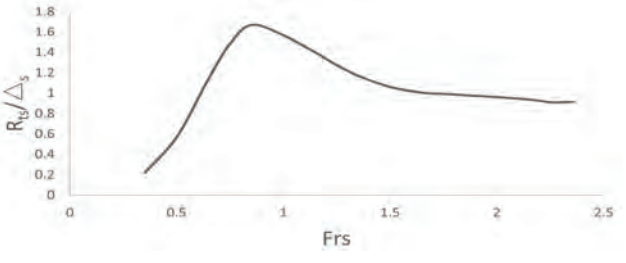

Fig. 19. Total resistance curve of stern demihulls

ANALYSIS OF WAVE-MAKING CHARACTERISTICS

Figs. 20 and 21 compare the contour and side view of the wave-making characteristics of the quadramaran and catamaran at different Froude numbers. It can be seen that, at low speed ($F_r < 0.53$), the two hulls turn from the displacement regime into the semi-planing regime. Both hulls descend and the dynamic trim angle increases. Transverse waves and divergent waves occur and reinforce each other, which makes the flow fields among the demihulls quite disorderly and adverse wave interference occurs. The flow in the stern region does not separate cleanly off the transom and therefore produces a large stern wake due to the sudden change in flow direction. Besides, the flows over the demihulls affect one another, which makes the flow asymmetric, so adverse viscous interference occurs. Having two more demihulls and a narrower separation than the catamaran results in complex flow fields, such that the quadramaran has worse wave and viscous interference and a higher wake, so that the total resistance of the quadramaran has a significant hump. Above the hump speed, as the hull rises and the dynamic trim angle decreases, the wave and viscous interference both improve, the flow fields gradually become orderly, the tail wake of the main hull extends backwards, the wake height decreases, and the flow under the transom is sufficient for separation. This results in cavitation being generated, which is equivalent to increasing the hull length and reducing the resistance, and the hydrodynamic force gradually dominates relative to the buoyancy force. As the hull of the quadramaran is separated in the middle by the bow and stern demihulls, the effect of the hydrodynamic force is greater than on the catamaran, so the total resistance of the quadramaran decreases in this regime, while for the catamaran it increases gently. Above the Froude number of 1.06, both hulls enter the planing regime. The wave pattern created behind the hulls is lengthened and narrower, and the length of cavitation becomes longer with the growth of the Froude number. The cavitation formed by the quadramaran is longer than that of the catamaran, and

the hydrodynamic force makes the quadramaran rise more, so the resistance curve is remarkably flat, while the wave-making at the bow of the catamaran rises, increasing its wave-making resistance, so the resistance curve is steep. In general, the quadramaran has worse wave-making characteristics at low speed but better characteristics at high speed compared to the catamaran.

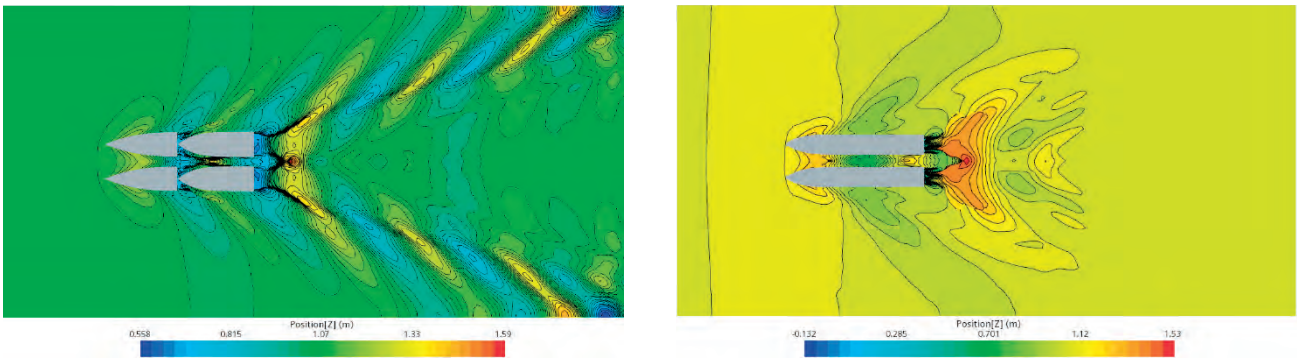

$F_r = 0.35$

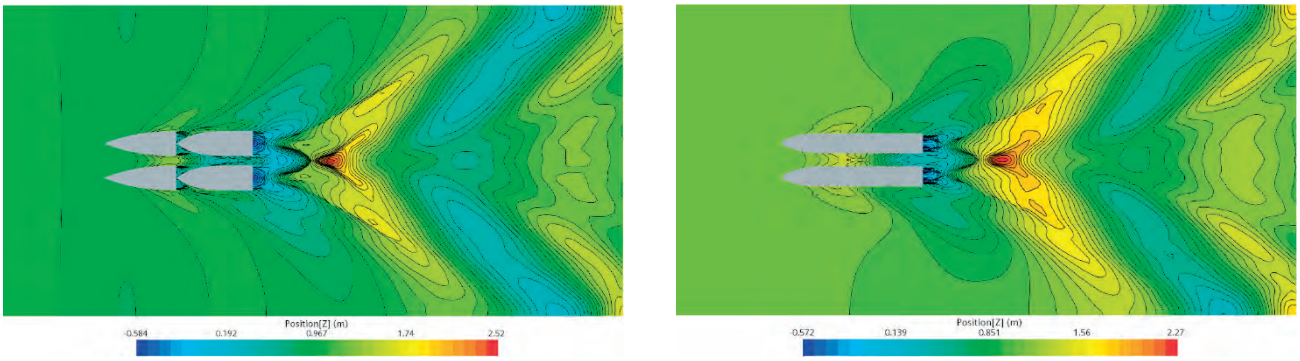

$F_r = 0.53$

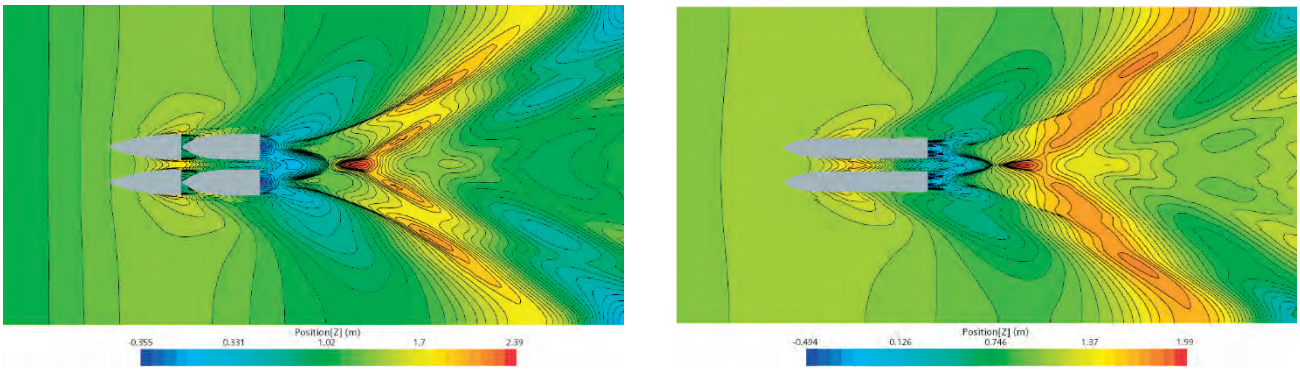

$F_r = 0.6$

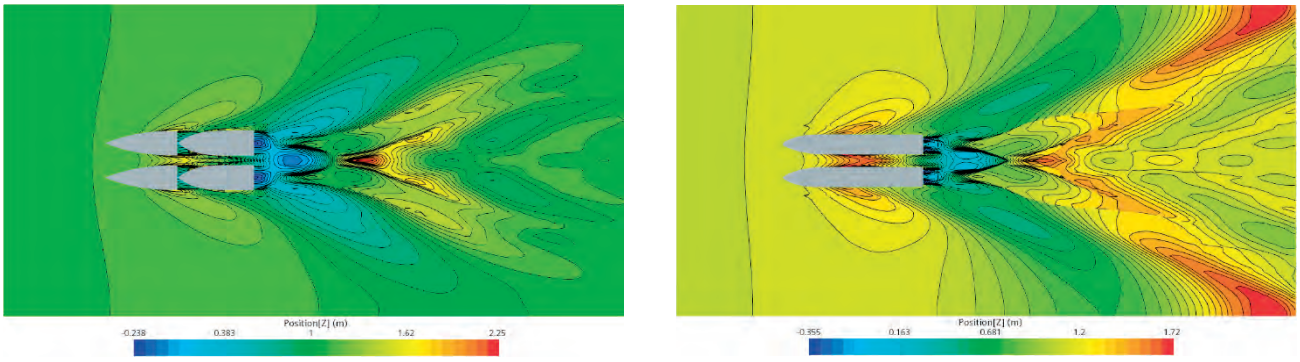

$F_r = 0.71$

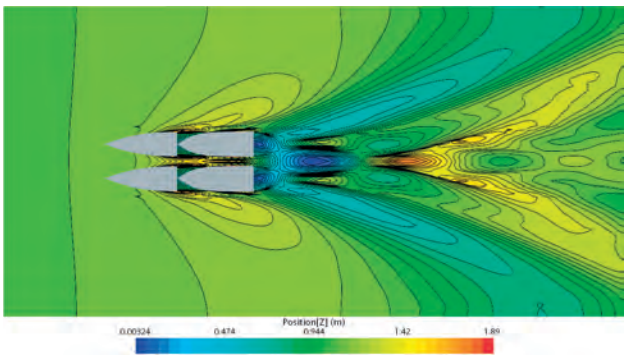

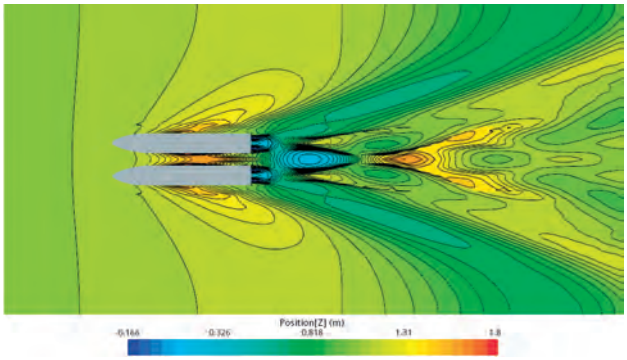

$F_r = 0.88$

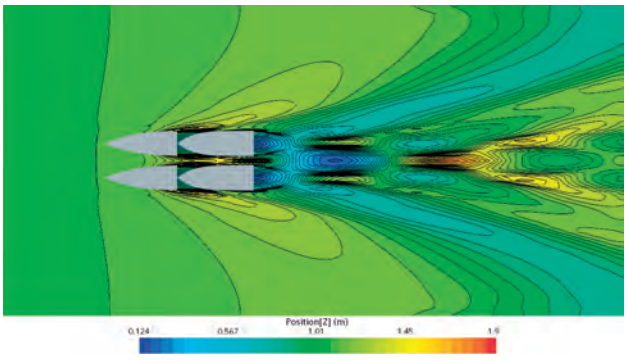

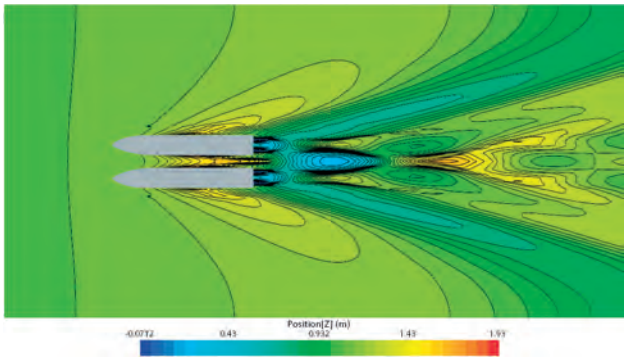

$F_r = 1.06$

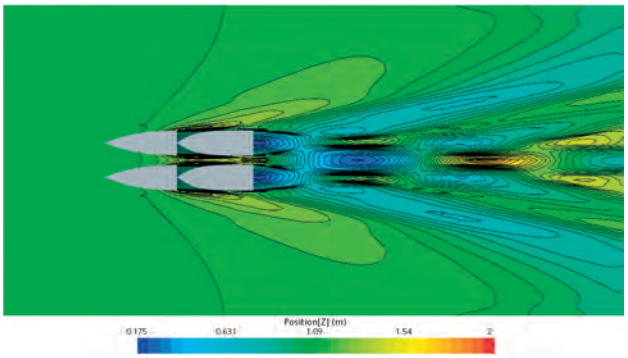

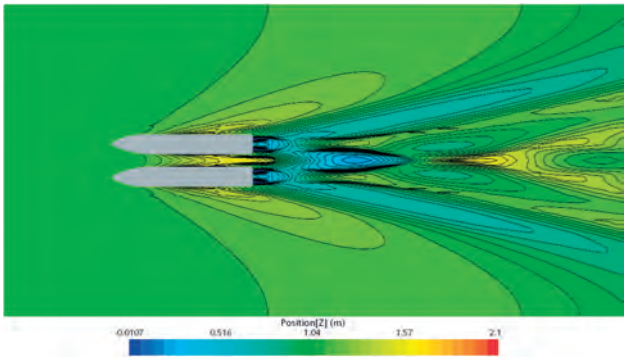

$F_r = 1.23$

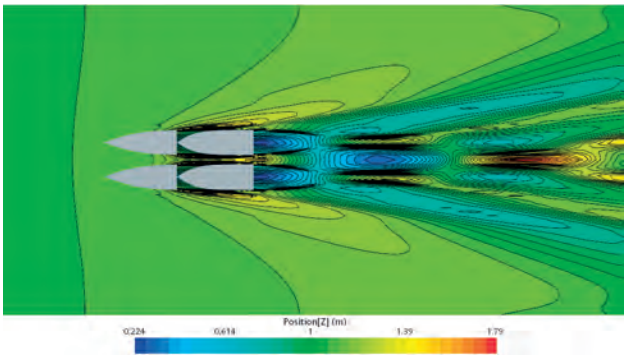

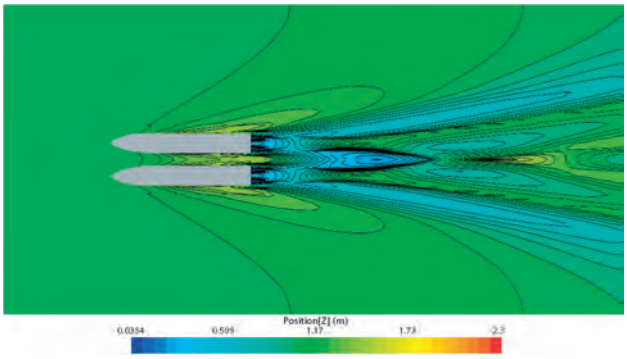

$F_r = 1.41$

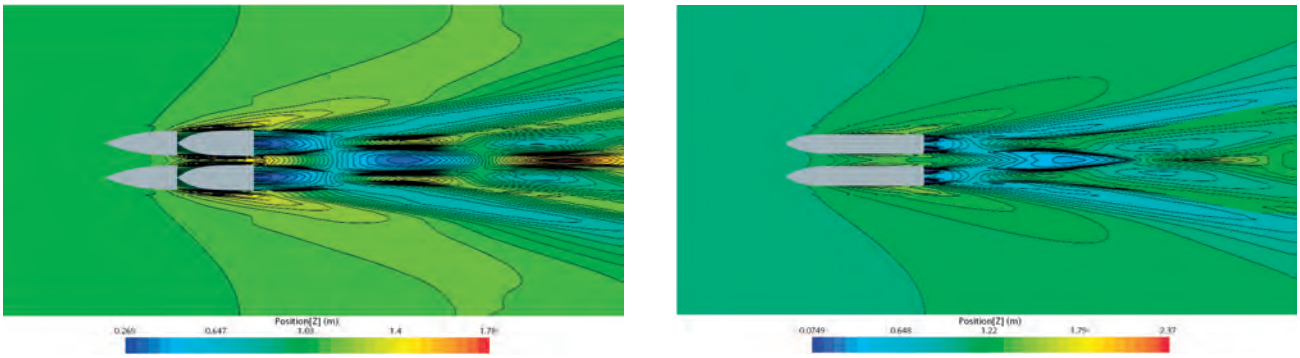

$F_r = 1.59$

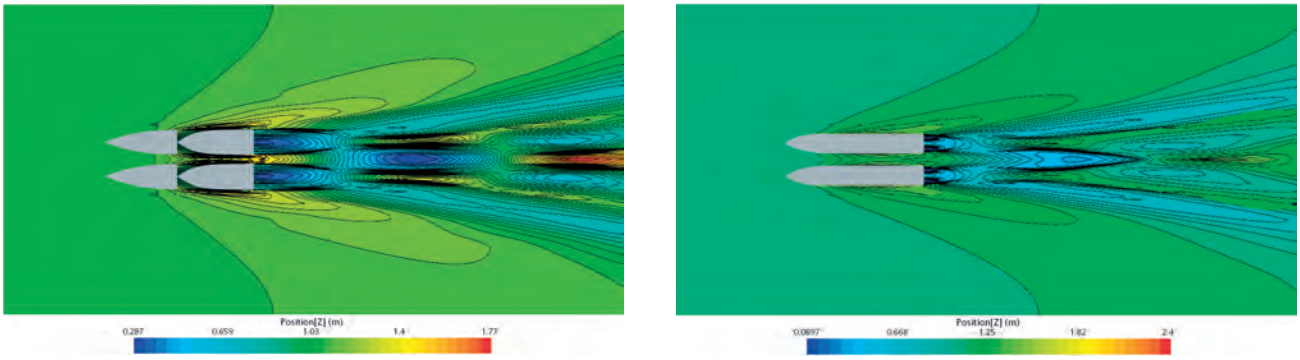

$F_r = 1.66$

(a) quadramaran *(b) catamaran*

Fig. 20. Wave contour comparison of two hulls at different F_r

$F_r = 0.35$

$F_r = 0.53$

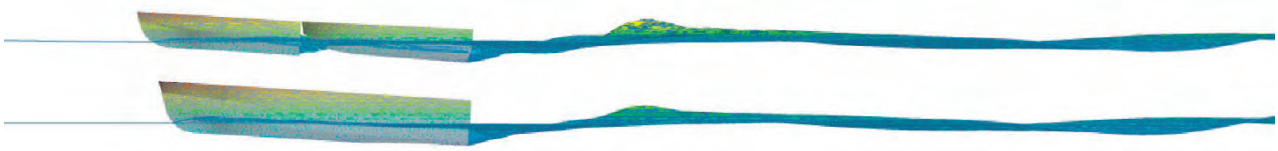

$F_r = 0.6$

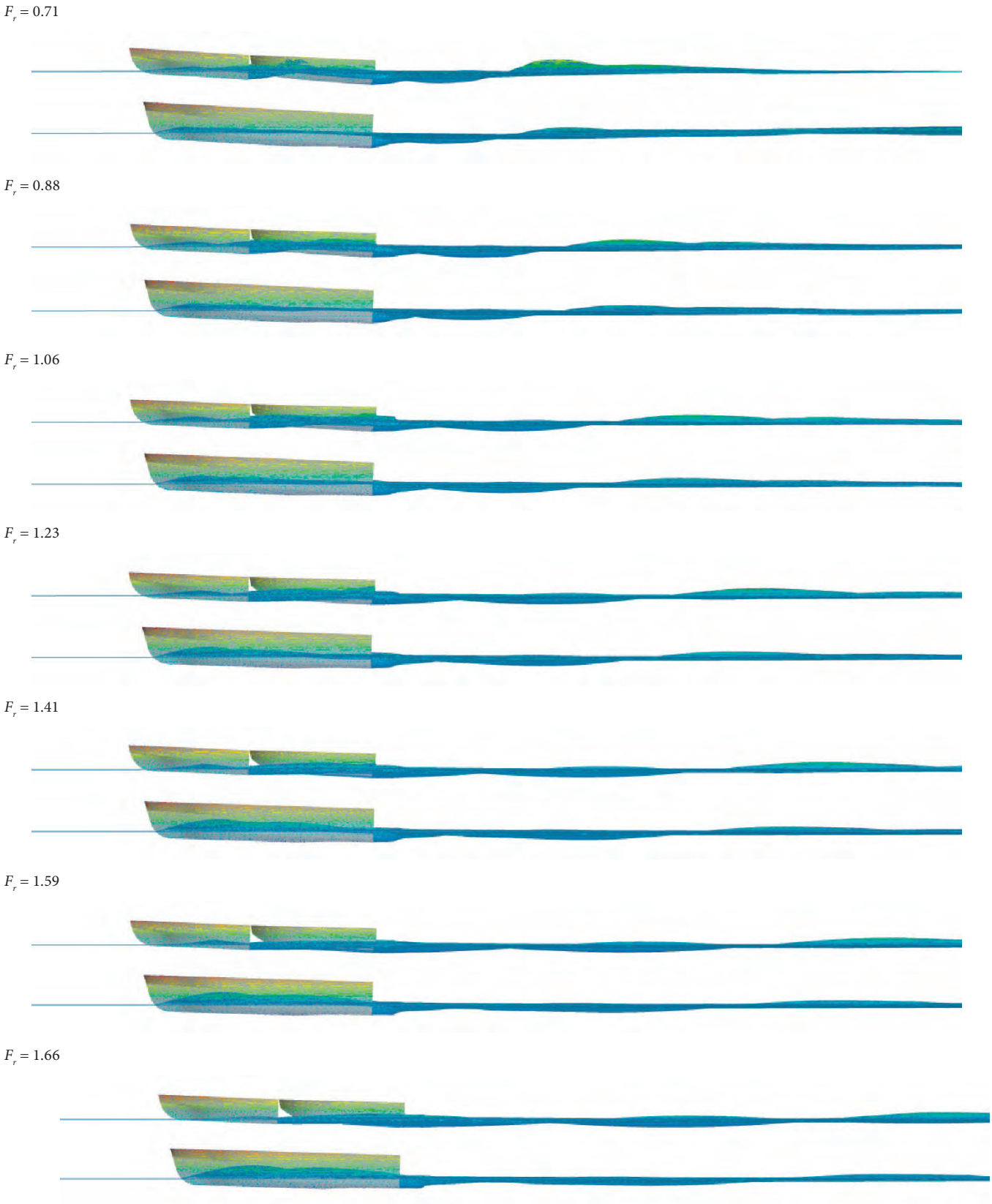

Fig. 21. Wave side view comparison of two hulls at different F_r

CONCLUSIONS

In this paper, a novel high-speed quadramaran is proposed, its resistance in calm water is calculated based on the CFD method, and the resistance characteristics are analysed. The following conclusions are obtained:

a) Due to the complex wave interference among the demihulls, the total resistance of the high-speed quadramaran has a significant hump at the Froude number of 0.6, the value of which is about 1.6 times that of the high-speed catamaran, for which the hump occurs at the Froude number of 0.53. Above the hump speed, the total resistance of the quadramaran does not increase but decreases, and the change trend of the total resistance tends to be flat when F_r = >1.06, which is different from that of the catamaran, where the total resistance curve was steep. The total resistance is significantly less than that of the catamaran, with a maximum reduction of 40% at the Froude number of 1.66, which indicates that the quadramaran has an obvious resistance advantage above the Froude number of 1.06 (at a service speed above 30 kn), and its high-speed performance is outstanding.

b) The frictional resistance curves of the quadramaran and catamaran have a similar change trend on account of the similar main scales of the two hulls. The residual resistance of the quadramaran first increases and then decreases with the increase of the Froude number. At low speed (F_r = < 0.53), the intricate wave interference of the quadramaran makes the hump value of residual resistance about 1.7 times that of the catamaran. However, at high speed (F_r = > 1.06), the residual resistance of the quadramaran is much less than that of the catamaran. This is mainly because, with the increase of the Froude number, the rise-up increases, the length of cavitation at the stern region is longer, and the wave interference is more favourable, which greatly reduces the wave-making resistance of the quadramaran.

c) The change trends of the frictional resistance on the bow and stern demihulls of the quadramaran are similar Both of them increase gradually as the Froude number rises, but the bow demihulls have lower values due to the smaller wetted surface. The change trends of the residual resistance on the bow and stern demihulls are also similar. Both of them increase first and then decrease with the growth of the Froude number, but the hump value of the stern is about 2 times that of the bow demihulls due to the intricate wave interference. The total resistance characteristics of the bow and stern demihulls are different. The total resistance of the bow demihulls increases gradually with the increase of the Froude number and has a small hump at the Froude number of 0.74. The total resistance of the stern demihulls first increases and then decreases with the increase of the Froude number and has a significant hump at the Froude number of 0.85 due to the complexity of the wave interference. Above the hump speed, as the hull rises and the wave interference changes from adverse to favourable, the total resistance of the stern demihulls decreases until reaching the Froude number of 1.51, when it tends to be flat.

ACKNOWLEDGEMENT

This work is supported by the Xiamen Natural Science Foundation (3502Z20227210) and Fujian Provincial Department of Education (JAT210227).

REFERENCES

1. J. L. Yang, H. B. Sun, X. W. Li, and X. Liu, "Flow field characteristic analysis of cushion system of partial air cushion support catamaran in regular waves," *Polish Maritime Research*, vol. 29, no. 3, pp. 35–46, 2022. doi: 10.2478/pomr-2022-0024.

2. J. L. Yang, Z. Lin, P. Li, Z. Q. Guo, H. B. Sun, and D. M. Yang, "Experimental investigations on the resistance performance of a high-speed partial air cushion supported catamaran," *International Journal of Naval Architecture and Ocean Engineering*, vol. 12, pp. 38–47, 2020. doi: 10.1016/j.ijnaoe.2019.05.004.

3. S. W. Kim, G. W. Lee, and K. C. Seo, "The comparison on resistance performance and running attitude of asymmetric catamaran changing shape of tunnel stern exit region," in *Proc. 1st International Joint Conference on Materials Science and Mechanical Engineering, Bangkok, Thailand, February 2018*. doi: 10.1088/1757-899X/383/1/012047.

4. A. Honaryar, M. Ghiasi, P. F. Liu, and A. Honaryar, "A new phenomenon in interference effect on catamaran dynamic response," *International Journal of Mechanical Sciences*, vol. 190, 106041, 2021. doi: 10.1016/j.ijmecsci.2020.106041.

5. H. Wang, R. C. Zhu, L. Zha, and M. X. Gu, "Experimental and numerical investigation on the resistance characteristics of a high-speed planing catamaran in calm water," *Ocean Engineering*, vol. 258, 11837, 2022. doi: 10.1016/j.oceaneng.2022.111837.

6. Z. S. Dong, X. P. Gao, W. C. Dong, and X. P. Lu, "Supercritical twin-planing-hull (in Chinese)," *Shipbuilding of China*, vol. 41, no. 3. pp. 1–7, Sep. 2000. doi: 10.3969/j.issn.1000-4882.2000.03.001.

7. H. X. Peng, *Numerical computation of multi-hull ship resistance and motion*. Ph.D. thesis, Dalhousie University, Canada, 2001. URI: http://hdl.handle.net/10222/55750.

8. B. Fang, X. P. Gao, and Z. S. Dong, "Performance of small waterplane area quad-hull's resistance (in Chinese)," *Journal of Naval University of Engineering*, vol. 15, no. 1, pp. 70–75, Feb. 2003. doi: 10.3969/j.issn.1009-3486.2003.01.018.

9. X. G. Cai, H. B. Chang, and P. Wang, "Research about the wave-making resistance of multi-hull ship in the calm water (in Chinese)," *Journal of Hydrodynamics*, vol. 24, no. 6, pp. 713–723, 2009. doi: 10.16076/j.cnki.cjhd.2009.06.009.

10. Y. Zhang, L. Chen, Z. Y. Zhang, F. Yang, and L. Zheng, "Research on resistance of multi-hull ships with FLUENT (in Chinese)," *Ship & Boat*, vol. 23, no. 5, pp. 23–30, Oct. 2012. doi: 10.3969/j.issn.1001-9855.2012.05.005.

11. X. W. Liu and D. C. Wan, "Numerical analysis of wave interference among demihulls of high-speed quadramarans (in Chinese)," *Shipbuilding of China*, vol. 58, Special Issue, pp. 140–151, Nov. 2017. [Online]. Available: http://qikan.cqvip.com/Qikan/Article/Detail?id=673742485&from=Qikan_Search_Index

12. Yanuar, Gunawan, A. Muhyi, and A. Jamaluddin, "Ship resistance of quadramaran with various hull position configurations," *Journal of Marine Science and Application*, vol. 15, pp. 28–32, 2016. doi: 10.1007/s11804-016-1340-3.

13. Yanuar, K. T. Waskito, and M. P. Widjaja, "Energy efficiency of high speed tetramaran ship model with minimum resistance configuration," *International Journal of Mechanical Engineering and Robotics Research*, vol. 6, no. 4, pp. 263–267, 2017. doi: 10.18178/ijmerr.6.4.263-267.

14. A. Farkas, N. Degiuli, and I. Martic, "Numerical investigation into the interaction of resistance components for a series 60 catamaran," *Ocean Engineering*, vol. 146, pp. 151–169, 2017. doi: 10.1016/j.oceaneng.2017.09.043.

15. J. F. Hu, Y. H. Zhang, P. Wang, and F. Qin, "Numerical and experimental study on resistance of asymmetric catamaran with different layouts," *Brodogradnja*, vol. 71, no. 2, pp. 91–110, 2020. doi: 10.21278/brod71206.

16. A. Ebrahimi, R. Shafaghat, A. Hajiabadi and M. Yousefifard, "Numerical and experimental investigation of the aero-hydrodynamic effect on the behavior of a high-speed catamaran in calm water," *Journal of Marine Science and Application*, vol. 21, pp. 56–70, 2022. doi: 10.1007/s11804-022-00295-6.

17. A. Li and Y. B. Li, "Numerical and experimental study on seakeeping performance of a high-speed trimaran with T-foil in head waves," *Polish Maritime Research*, vol. 26, no. 3, pp. 65–77, 2019. doi: 10.2478/pomr-2019-0047.

18. M. Heidari, Z. Razaviyan, F. Yusof, E. Mohammadian, A. B. Alias, M. H. Akhbari, A. Akbari, and F. Movahedi, "Numerical analysis of side hull configuration in trimaran," *Revista Internacional de Métodos Numéricos para Cálculo y Diseño en Ingeniería*, vol. 35, no. 2, pp. 1–31, 2019. doi: 10.23967/j.rimni.2019.06.004.

19. B. Yildiz, B. Sener, S. Duman, and R. Datla, "A numerical and experimental study on the outrigger positioning of a trimaran hull in terms of resistance," *Ocean Engineering*, vol. 198, 106938, 2020. doi: 10.1016/j.oceaneng.2020.106938.

20. A. Nazemian and P. Ghadimi, "CFD-based optimization of a displacement trimaran hull for improving its calm water and wavy condition resistance," *Applied Ocean Research*, vol. 113, 102729, 2021. doi: 10.1016/j.apor.2021.102729.

21. J. D. Anderson, *Computational Fluid Dynamics: The Basics with Applications.* New York: McGraw-Hill, 1995.

22. J. H. Ferziger, M. Perić, and R. L. Street, *Computational Methods for Fluid Dynamics*, 4th ed. 2020 Edition. Springer, 2019.

23. User Guide, 2022. STAR CCM+ version 2022. SIEMENS Simcenter.

24. K. V. Meredith, A. Heather, J. de Vries, and Y. Xin, "A numerical model for partially-wetted flow of thin liquid films," *Computational Methods in Multiphase Flow VI*, vol. 70, pp. 239–250, 2011. doi:10.2495/MPF110201.

25. H. Kazemi, M. M. Doustdar, A. Najafi, H. Nowruzi, and M. J. Ameri, "Hydrodynamic performance prediction of stepped planing craft using CFD and ANNs," *Journal of Marine Science and Application*, vol. 20, pp. 67–84, 2021. doi.org/10.1007/s11804-020-00182-y.

26. P. Ghadimi, S. M. Sajedi, and M. Sheikholeslami, "Experimental study of the effects of V-shaped steps on the hydrodynamic performance of planing hulls," *Journal of Engineering for the Maritime Environment*, vol. 237(1), pp. 238–256, 2023. doi: 10.1177/14750902221098304.

27. ITTC, 2021. *Recommended Procedures and Guidelines. Uncertainty Analysis in CFD Verification and Validation Methodology and Procedures*. 7.5-03-01-01.

28. ITTC, 2017. *Recommended Procedures and Guidelines. Uncertainty Analysis in CFD, Examples for Resistance and Flow*. 7.5-03-02-01.

29. L. Birk, *Fundamentals of Ship Hydrodynamics: Fluid Mechanics, Ship Resistance and Propulsion*. UK, Chichester: John Wiley, 2019.

30. ITTC, 2014. *Recommended Procedures and Guidelines. Practical Guidelines for Ship CFD Applications*. 7.5-03-02-03.

31. Z. H. Liu, W. T. Liu, Q. Chen, F. Y. Luo, and S. Zhai, "Resistance reduction technology research of high-speed ships based on a new type of bow appendage," *Ocean Engineering*, vol. 206, 107246, 2020. doi.org/10.1016/j.oceaneng.2020.107246.

32. O. Faltinsen, *Hydrodynamics of High-Speed Marine Vehicles*. Cambridge University Press, 2010.